Computer Modeling in Engineering & Sciences

Tech Science Press

Doi:10.32604/cmes.2025.070524

ARTICLE

Energy Transfer during Strong Oscillations of a Spherical Bubble with Non-Ideal Gas Equations of State

Minki Kim[1] **and Jenny Jyoung Lee**[2,*]

[1]Center for Fluid Mechanics, School of Engineering, Brown University, Providence, RI 02903, USA
[2]Department of Data Science, Ewha Womans University, Seoul, 03760, Republic of Korea

*Corresponding Author: Jenny Jyoung Lee. Email: jj_lee@ewha.ac.kr

Received: 18 July 2025; Accepted: 16 September 2025; Published: 30 October 2025

ABSTRACT: Spherical bubble oscillations are widely used to model cavitation phenomena in biomedical and naval hydrodynamic systems. During collapse, a sudden increase in surrounding pressure initiates the collapse of a cavitation bubble, followed by a rebound driven by the high internal gas pressure. While the ideal gas equation of state (EOS) is commonly used to describe the internal pressure and temperature of the bubble, it is limited in its capacity to capture molecular-level effects under highly compressed conditions. In the present study, we employ non-ideal EOS for the gas (the van der Waals EOS and its volume-limited case) to investigate bubble oscillations with a focus on energy redistribution. Bubble oscillation is modeled in two phases: collapse, described by the Keller–Miksis formulation, and rebound, where peak shock pressure is estimated using similitude-based relations. To assess the role of EOS in energy redistribution, we introduce a framework that quantifies energy components in the bubble–liquid system while conserving total energy, tailored to each EOS. Using this framework, we evaluate energy concentration, acoustic radiation, and shock propagation and statistically analyze their dependence on both the driving pressure and the EOS of gas. We statistically derive scaling relations of key bubble dynamics quantities, energy concentration and radiation, and shock pressure using the driving pressure ratio. This work provides a generalizable framework and set of scaling relations for predicting bubble dynamics and energy transfer, with potential applications in evaluating the impacts of cavitation phenomena in complex practical systems.

KEYWORDS: Cavitation bubble; van der Waals equation of state; spherical bubble oscillations

1 Introduction

Cavitation bubbles play a key role in various industrial and biomedical applications, including naval hydrodynamic machinery [1–3], histotripsy [4], lithotripsy [5,6], chemical processing [7], cancer ablation [8], and coated micro-bubbles for drug delivery [9,10]. When subjected to high ambient pressure compared to the gas pressure inside the bubble, it undergoes rapid oscillations that may emit shock waves into the surrounding medium. These shocks can induce localized high-pressure and stress regions, which may potentially induce damage on nearby objects or the medium [11–13]. Such effects can be harnessed for beneficial outcomes in targeted applications such as breaking kidney stones, ablating cancer cells, or initiating chemical reactions; but they may also be detrimental. In naval machinery, repeated bubble collapses near solid objects can cause erosion, ultimately reducing the structural integrity [1,14].

A cavitation bubble behaves asymmetrically when located near a solid surface [15]. While the bubble dynamics are nearly spherical in the early stages of collapse, asymmetries rapidly develop due to imbalances

in mass and momentum transport near the boundary. This results in non-spherical bubble deformation and the formation of a high-speed re-entrant jet directed from the side farther from the boundary toward the side close to the boundary [16,17]. When the jet impacts the opposite side of the bubble near the boundary, a water-hammer shock is generated, further compressing the bubble and emitting secondary shock waves [13]. These shocks induce localized high pressures and stresses on nearby surfaces, potentially causing material damage and surface erosion—a common source of wear in engineering systems [18]. Despite its importance, simulating these phenomena still remains challenging due to the complexity of bubble-boundary [19–22] and bubble-bubble [23,24] interactions.

A spherical bubble setting is often used as an idealized framework that captures key features of non-spherical bubble dynamics [25–27]. Under symmetric conditions, the bubble collapses and rebounds spherically. During collapse, the potential energy stored in the surrounding liquid is transferred into kinetic energy, which is ultimately concentrated into the bubble as internal energy. While this energy redistribution process is well understood in the incompressible limit, it remains less explored when compressibility and the associated wave generation are taken into account [28,29]. In particular, for strong oscillations, compressibility effects become increasingly significant and must be incorporated to accurately describe energy transfer and energy radiation via waves.

Under such oscillations, the gas behavior inside the bubble deviates significantly from ideal gas assumptions, making molecular effects non-negligible. As the driving pressure increases, the bubble undergoes more violent collapse, enhancing the influence of intermolecular forces and finite molecular volume. These non-ideal gas effects are particularly important in sonochemistry and sonoluminescence, both of which require large compression ratios to initiate chemical reactions and light emission [7,30,31]. During the turnaround from collapse to rebound, the bubble reaches extreme conditions: pressures on the order of 4,000–8,000 atm and temperatures approaching 15,000 K for argon, with several molecular emission estimates suggesting peaks near 30,000 K [32,33]. For Ar–Ne mixtures, the sonoluminescence temperature is reduced to around 1,500 K [34]. Although these extreme conditions last only $O(0.1)$ μs, they are sufficient to trigger sonochemical reactions and light emission. Indeed, during such short intervals, molecular effects strongly influence bubble dynamics, altering energy partitioning and shock generation, which are critical for understanding the initiation of chemical reactions and light emission, as well as cavitation-induced damage. However, quantifying individual energy components under these conditions remains challenging due to the complexity introduced by non-ideal thermodynamic gas behavior.

To model non-ideal gas effects, various equations of state (EOS) have been employed to describe the gas pressure inside a collapsing bubble. For low-to-moderate amplitude oscillations, the ideal gas law is typically sufficient [35–37]. However, under strong oscillations, the van der Waals EOS is often used to account for intermolecular attractive forces and finite molecular volume, both of which become significant during violent collapse [31]. As an alternative, the ideal gas law with a volume cutoff has been applied to approximate the effects of the van der Waals core volume [30,38]. These EOS formulations are commonly coupled with Rayleigh–Plesset-type equations [15,39,40] to model the evolution of pressure and temperature inside the bubble during oscillations. However, the energy transfer associated with different EOS models has not been thoroughly investigated.

In the present study, we develop an energy budget framework for bubble oscillations, particularly under strong oscillations, tailored to different EOS while ensuring conservation of total energy in the bubble–liquid system. We specifically investigate how non-ideal EOS (van der Waals and its volume-limited form) affect bubble compression, energy redistribution, and shock emission. By combining this framework with statistical analysis, we establish new scaling relations linking driving pressure to bubble dynamics, energy concentration, and shock pressure. These contributions provide new insights into the role

of molecular effects in cavitation dynamics and offer predictive tools for assessing cavitation-induced energy transfer in practical applications. The article is organized as follows. Section 2 introduces the EOS and bubble dynamics models. Section 3 introduces the energy budget framework, which is applied in Section 4 to analyze bubble dynamics and energy redistribution. Section 5 summarizes the overall findings of the present study, discusses the limitations of the framework, and outlines potential directions for future research.

2 Methods

In this section, we introduce the EOS and bubble dynamics model used to simulate spherical bubble oscillations under varying driving pressures.

2.1 Equation of State for the Gas inside the Bubble

We employ three different EOS to investigate molecular effects on bubble dynamics, as well as the resulting energy redistribution, acoustic radiation, and shock wave emission. First, we use the full van der Waals EOS [31]:

$$\left(p_b + \frac{n_b^2 a_{\text{van}}}{V^2}\right)(V - n b_{\text{van}}) = n_b R_b T_b, \tag{1}$$

where p_b is the bubble pressure, n_b is the number of moles of gas, a_{van} is the correction factor for intermolecular attraction, V is the bubble volume, b_{van} is the correction factor for finite molecular size, R_b is the universal gas constant, and T_b is the bubble temperature. The second model incorporates only the finite molecular volume through the van der Waals hard-core correction, referred to as the volume-limited van der Waals EOS [30,41]:

$$p_b\,(V - V_{\text{van}}) = n_b R_b T_b, \tag{2}$$

where V_{van} is the hard core volume. As a reference case, we also consider the ideal gas law, which is recovered by setting $V_{\text{van}} = 0$ in Eq. (2).

We compare bubble pressures predicted by the three EOS models across a range of bubble volumes starting from the initial volume and decreasing toward smaller values (Fig. 1). For larger bubble volumes, corresponding to the early stages of collapse, all three models yield nearly identical pressures. However, as the bubble compresses to around 2 % of its initial volume, the van der Waals EOS shows higher pressures than the ideal gas law. This can be attributed to the finite molecular volume core becoming significant relative to the total bubble volume, increasing the effective pressure compared to the ideal gas case that neglects this volume. At volumes below 1 % of the initial value, the full van der Waals EOS begins to show lower bubble pressures than the volume-limited version, as intermolecular attractive forces reduce the overall gas pressure.

During oscillations, the bubble pressure is assumed to follow an adiabatic law, which is appropriate for violent collapses where the timescale of thermal diffusion is orders of magnitude longer than that of the bubble collapse [42–44]. For each EOS, the corresponding adiabatic relation can be expressed as:

$$\left(p_b + \frac{n_b^2 a_{\text{van}}}{V^2}\right)(V - n b_{\text{van}})^{\gamma} = C_{o,1}, \tag{3}$$

for the full van der Waals EOS, and

$$p_b\,(V - V_{\text{van}})^{\gamma} = C_{o,2}, \tag{4}$$

for the volume-limited van der Waals EOS, where γ is the specific heat ratio. Here, $C_{o,1}$ and $C_{o,2}$ are constants determined from the reference state conditions at $p_{b,o}$ and $T_{b,o}$. For the ideal gas EOS, $V_{\text{van}} = 0$ in Eq. (4).

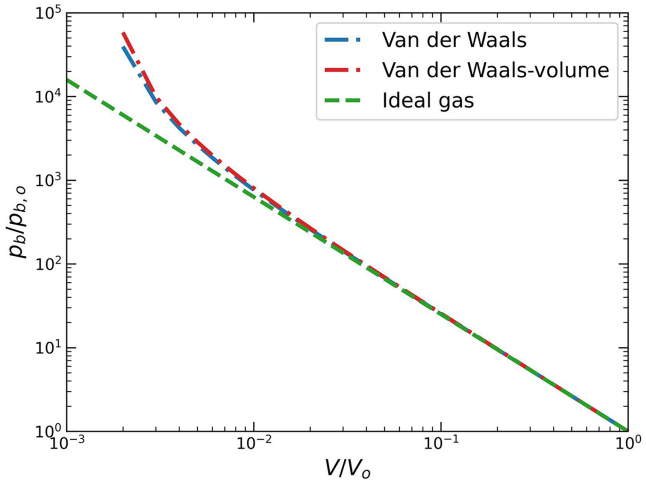

Figure 1: Pressure inside a bubble as a function of bubble volume for different equations of state: (blue dash-dotted line) van der Waals equation, (red dash-dotted line) volume-limited van der Waals equation, and (green dashed line) ideal gas law

2.2 Spherical Bubble Dynamics

A spherical bubble with an initial radius R_o is assumed to be in equilibrium in a weakly compressible liquid, such that the pressure across the bubble–liquid interface is balanced. The initial bubble pressure is approximately $p_{b,o} = 1$ atm at a temperature $T_{b,o} = 300$ K. The bubble, bounded by domain Ω_b, is subjected to an instantaneous increase in surrounding liquid pressure Δp, initiating collapse, such that the far-field pressure becomes $p_\infty = p_{b,o} + \Delta p$ in domain Ω_∞ (Fig. 2). The resulting bubble oscillations in a weakly compressible liquid are governed by the Keller–Miksis equation [40]:

$$R\ddot{R}\left(1-\frac{\dot{R}}{c_l}\right)+\frac{3}{2}\dot{R}^2\left(1-\frac{\dot{R}}{3c_l}\right)=\frac{p_l(R)-p_\infty}{\rho_l}\left(1+\frac{\dot{R}}{c_l}\right)+R\frac{\dot{p}_l(R)}{\rho_l c_l}, \tag{5}$$

where R is the bubble radius, the dot operator is the time derivative, c_l is the speed of sound in the liquid, $p_l(R)$ is the liquid pressure at the bubble wall, and ρ_l is the liquid density. The wall pressure is given by $p_l(R) = p_b - 4\mu_l\dot{R}/R - 2\sigma/R$, where μ_l is the liquid viscosity and σ is the surface tension. The initial bubble-wall velocity is set to $\dot{R}_o = \Delta p/\rho_l c_l$ [15], to represent an instantaneous pressure increase, an idealized case of shock-induced collapse with rapid shock propagation. The driving pressure ratio $\Delta p/p_{b,o}$ ranges from 0.6 to 10^4, covering conditions relevant to shock-induced collapse [45,46] and underwater explosions [47–49]. Detailed problem parameters are listed in Table 1. For normalization, R_o and $\sqrt{\Delta p/\rho_l}$ are used as the characteristic length and velocity scales, respectively. The Reynolds and Weber numbers are on the order of $O(10^3)$–$O(10^5)$ and $O(10^2)$–$O(10^6)$, respectively, indicating that viscous and surface tension effects are negligible for micro-to-millimeter-size bubbles. As a result, viscosity and surface tension are not considered in the present analysis, and the bubble and liquid pressures are assumed to be equal at the bubble wall. For the bubble dynamics simulations, Eq. (5) is coupled with different EOS (Eqs. (3) and (4)) and solved using a fourth-order Runge-Kutta time-integration scheme with adaptive time stepping [50].

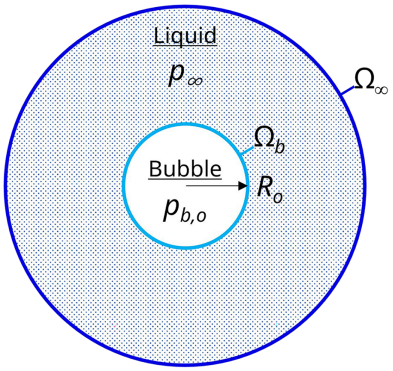

Figure 2: Schematic of the initial configuration for the bubble collapse problem

Table 1: List of parameters used in the bubble dynamics models and EOS

Symbol	Parameter name	Value
$p_{b,o}$	Initial bubble pressure	1.01325×10^5 Pa
$T_{b,o}$	Initial bubble temperature	300 K
R_o	Initial bubble radius	0.5×10^{-3} m
Δp	Driving pressure	5.8×10^4–1.0×10^9 Pa
ρ_l	Density (liquid)	998 kg/m^3
c_l	Speed of sound (liquid)	1510 m/s
γ	Specific heat ratio (air)	1.4
a_{van}	Van der Waals constant (air)	0.137 Pa·m^6/mol^2
b_{van}	Van der Waals constant (air)	3.7×10^{-5} m^3/mol
V_{van}	Volume-limited van der Waals constant (air)	8.4×10^{-13} m^3
c_v	Molar heat capacity (air)	20.8 J/mol·K
R_b	Universal gas constant	8.314 J/mol·K
n_b	Number of moles	2.1×10^{-8} mol

Bubble dynamics exhibit distinct behaviors at high driving pressure ratios depending on the EOS considered. Fig. 3 presents the time evolution of the normalized bubble radius R/R_o and normalized bubble-wall velocity $\dot{R}^*$ for different EOS cases. Each quantity is normalized by the characteristic length and velocity scales. At a low driving pressure ratio of $\Delta p/p_{b,o} = 9$, all three EOS produce nearly identical results for both the bubble radius and bubble-wall velocity. However, At a high driving pressure ratio of $\Delta p/p_{b,o} = 10^3$, the presence of a molecular volume core limits bubble compression in the final stages of collapse, resulting in a reduced bubble-wall velocity. The two van der Waals EOS cases exhibit similar trends, indicating the dominant role of molecular volume effects compared to intermolecular attractive forces under highly compressed conditions.

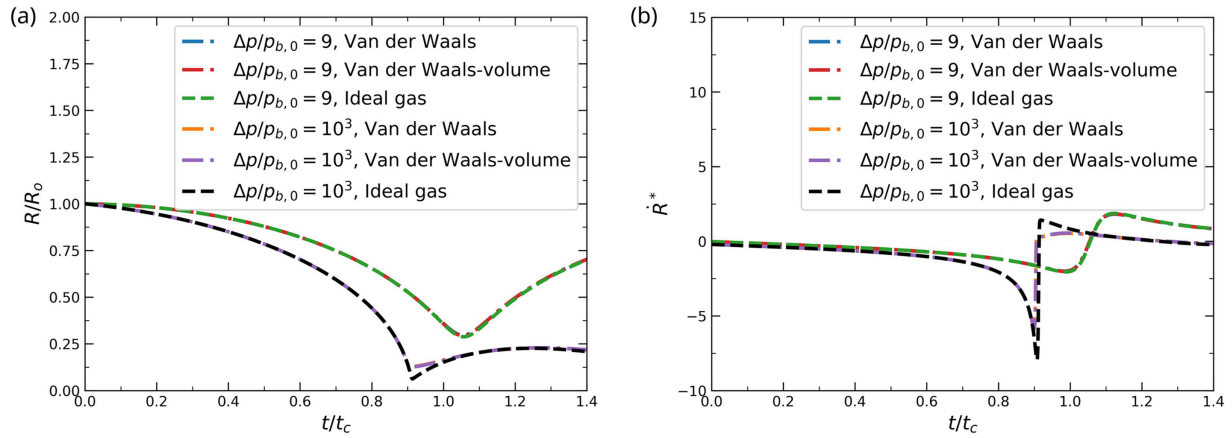

Figure 3: Time evolution of (**a**) normalized bubble radius and (**b**) normalized bubble-wall velocity for the full van der Waals EOS, the volume-limited van der Waals EOS, and the ideal gas EOS at different driving pressure ratios of $\Delta p/p_{b,o} = 9$ and 10^3

3 Energy Component Quantification in the Bubble–Liquid System

We quantify the energy components of the bubble–liquid system for different EOS. We specifically focus on ensuring conservation of total energy for different EOS cases by accurately computing the bubble internal energy and the radiated energy during bubble collapse and rebound. In the current bubble dynamics model, four energy components are considered: internal energy of the bubble (E_{BIE}), acoustic radiation energy (E_{ARE}), potential energy of the liquid (E_{LPE}), and kinetic energy of the liquid (E_{LKE}). The total energy is thus given by: $E_{\mathrm{TE}} = E_{\mathrm{BIE}} + E_{\mathrm{ARE}} + E_{\mathrm{LPE}} + E_{\mathrm{LKE}}$ (Fig. 4a). We improve the formulation of the bubble internal energy to make it consistent with each EOS and revise the acoustic radiated energy form to remain compatible with the modified internal energy formulation.

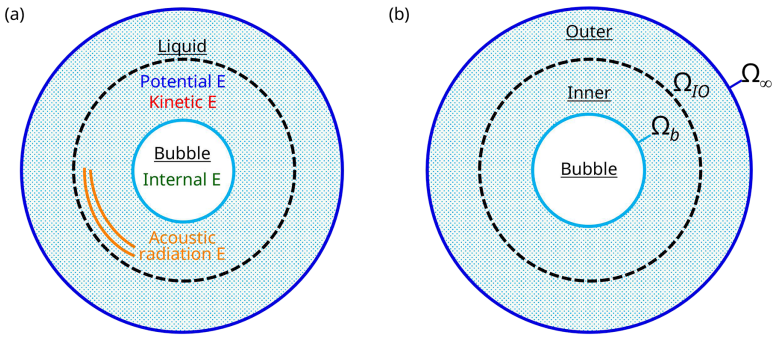

Figure 4: Schematics of the energy budget framework: (**a**) energy components in the bubble–liquid system and (**b**) inner and outer regions of the weakly compressible liquid

The internal energy of the bubble is defined as $E_{\mathrm{BIE}} = \int \rho_b C_v T_b dV$, where ρ_b is the bubble gas density and C_v is the specific heat at constant volume. For the van der Waals EOS, the internal energy is expressed as:

$$E_{\mathrm{BIE,van}} = \left(p_b + \frac{n_b^2 a_{\mathrm{van}}}{V^2}\right)\left(\frac{V - nb_{\mathrm{van}}}{\gamma - 1}\right) - \frac{n_b^2 a_{\mathrm{van}}}{V}, \tag{6}$$

and for the volume-limited van der Waals EOS:

$$E_{\mathrm{BIE,van,vol}} = p_b \left(\frac{V - V_{\mathrm{van}}}{\gamma - 1} \right), \tag{7}$$

for the ideal gas EOS, the volume correction vanishes, i.e., $V_{\mathrm{van}} = 0$ in Eq. (7).

We quantify the energy radiated acoustically during bubble oscillations in a weakly compressible liquid based on the first-order theory by [51], extended to the energy budget framework in [28,29]. In a weakly compressible liquid, the liquid domain can be divided into two sub-regions based on characteristic length scales. The inner region, enclosed by Ω_b and Ω_{IO} (Fig. 4b), is nearly incompressible due to the rapid response of the liquid to bubble motion. In contrast, the outer region, extending from Ω_{IO} to Ω_∞, is weakly compressible because the propagation of pressure disturbances requires finite time. The characteristic length scale of the inner region is approximately R_o, while that of the outer region is $R_o c_l/\sqrt{(\Delta p/\rho_l)}$, leading to the dimensionless parameter $\varepsilon = \sqrt{(\Delta p/\rho_l)}/c_l$. Based on this separation of scales, the liquid pressure in the inner region can be expressed to first order in ε [28,29,51]:

$$p_l(r) = p_\infty + \rho_l \frac{\ddot{V}}{4\pi r} - \rho_l \frac{\dot{V}^2}{32\pi^2 r^4} - \frac{\rho_l}{c_l} \frac{\dddot{V}}{4\pi} + O(\varepsilon^2), \tag{8}$$

where r is the radial coordinate from the bubble center. The first three terms represent hydrodynamic contributions, which can be derived in the incompressible limit using the Rayleigh-Plesset equation [39,52], while the last term implies the acoustic perturbation p_{ac}. The third-order derivative in Eq. (8) can lead to divergent solutions, a known issue in linear acoustic theory [53,54]. To avoid this, it is common to approximate $\dddot{V}$ using lower-order derivatives as follows [40,51]:

$$\dddot{V} \approx 4\pi \left[\frac{\dot{R}^3}{2} + R\dot{R}\ddot{R} + \dot{R} \left(\frac{p_l(R) - p_\infty}{\rho_l} \right) + R \frac{\dot{p}_l(R)}{\rho_l} \right]. \tag{9}$$

The radiated energy via acoustic waves is then calculated at the outer boundary of the inner region, which is assumed to be sufficiently far from the bubble:

$$E_{\mathrm{ARE}} = \int_0^t \lim_{\Omega_{\mathrm{IO}} \to \infty} \int_{\Omega_{\mathrm{IO}}} p_{\mathrm{ac}} u_l(r) dt, \tag{10}$$

where $u_l(r)$ is the liquid velocity at radial position r. Substituting Eqs. (3), (4), (8), and (9) into Eq. (10) yields the acoustic radiation energy. Note that the liquid pressure at the bubble-wall, $p_l(R)$, depends on the EOS, resulting in different approximations of $\dddot{V}$ in Eq. (8).

The potential energy of the liquid, associated with the far-field pressure, is given by [55]:

$$E_{\mathrm{LPE}} = p_\infty V, \tag{11}$$

which reflects energy stored in the system due to a conservative force field, independent of the bubble oscillation history. The kinetic energy of the liquid in the inner region can be expressed as [56]:

$$E_{\mathrm{LKE}} = \frac{\rho_l}{2} \int_{\Omega_b \cup \Omega_{IO}} \phi_l \frac{\partial \phi_l}{\partial n} dS = 2\pi \rho_l R^3 \dot{R}^2, \tag{12}$$

where ϕ_l is the velocity potential in the liquid.

We analyze the time evolution of energy components at $\Delta p/p_{b,o} = 9$ and 10^3 to investigate energy transfer under weak and strong bubble oscillations (Fig. 5). We only show the volume-limited van der Waals

EOS (Eq. (2)), which yields results similar to those from the full van der Waals EOS (Eq. (1)). Note that each energy component is normalized by the initial total energy. In general, as the bubble collapses, the potential energy of the liquid (Eq. (11)) is transferred to liquid kinetic energy (Eq. (12)), which is finally concentrated into the bubble as internal energy (Eq. (6) or (7)). During this process, interfacial motion perturbs the surrounding liquid, generating outward-propagating acoustic perturbations that carry radiated energy. At a low driving pressure ratio $\Delta p/p_{b,o} = 9$, most of the initial energy stored in the liquid is concentrated to the bubble, with negligible loss through acoustic radiation (Fig. 5a). In contrast, at a high driving pressure ratio $\Delta p/p_{b,o} = 10^3$, a large portion of the initial energy, primarily stored as potential energy, is radiated away via acoustic perturbations. As a result, less energy is concentrated in the bubble, and a smaller amount of energy remains in the system during the rebound phase (Fig. 5b).

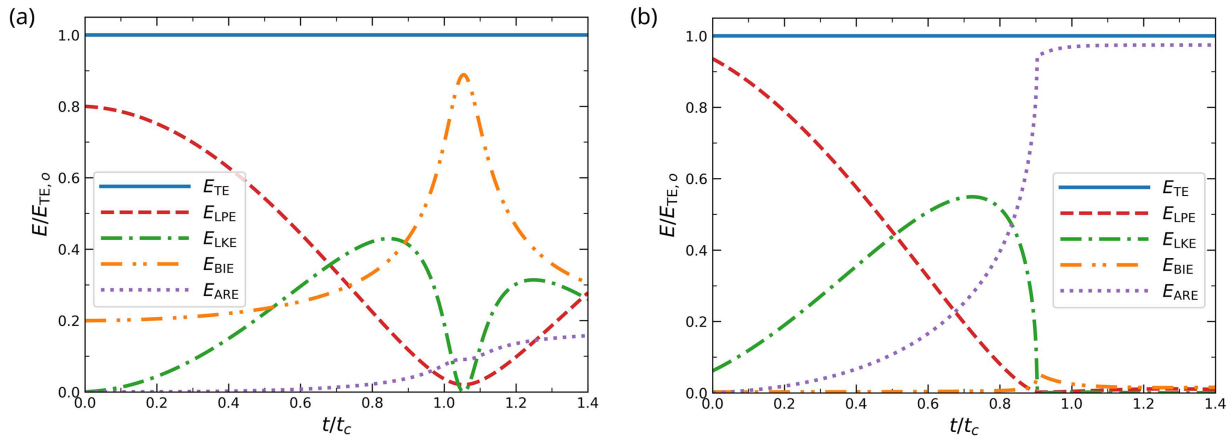

Figure 5: Time evolution of energy components, normalized by the initial total energy $E_{TE,o}$, during bubble collapse and rebound for the volume-limited van der Waals EOS at different driving pressure ratios of $\Delta p/p_{b,o}$ = (**a**) 9 and (**b**) 10^3: (blue solid lines) E_{TE}, (red dashed lines) E_{LPE} (Eq. (11)), (green dash-dotted lines) E_{LKE} (Eq. (12)), (orange dash-double-dotted lines) E_{BIE} (Eq. (7)), and (purple dotted lines) E_{ARE} (Eq. (10))

4 Results

In this section, we model bubble oscillation as comprising two phases: (i) the collapse phase, during which the bubble compresses from its initial state to its minimum radius, and (ii) the rebound phase, during which shock waves are emitted and propagated outward. The Keller–Miksis formulation is employed during the collapse phase to evaluate energy concentration and redistribution as a function of the driving pressure ratio. During the rebound phase, we estimate shock propagation using a theoretical relation based on the Kirkwood–Bethe hypothesis [57], which relates the bubble pressure and radius at the instant of collapse to the shock properties. Based on this relation, we analyze the relationship between the peak shock pressure and the driving pressure ratio.

We compare the collapse and rebound phases for different EOS over a wide range of driving pressure ratios. Based on this comparison, we statistically classify low and high driving pressure regimes that lead to different behaviors in bubble dynamics, energy transfer, and shock propagation. We fit linear regression models relating key bubble and shock quantities to the driving pressure ratio and assess how these trends differ statistically across EOS cases.

4.1 Bubble Dynamics during the Collapse Phase

We analyze the bubble volume at collapse, collapse time, and maximum bubble-wall velocity for different EOS cases (Fig. 6). In all cases, these bubble quantities exhibit similar trends at low driving pressure ratios

up to $\Delta p/p_{b,o} \approx 40$. As the driving pressure increases, the results for the van der Waals EOS begin to deviate largely from those of the ideal gas EOS, due to the increasing importance of molecular effects. Specifically, the bubbles are less compressed in the van der Waals EOS cases compared to the ideal gas EOS (Fig. 6a). For $\Delta p/p_{b,o} \geq 100$, the normalized bubble volumes at collapse remain on the order of $O(10^{-3})$ for both van der Waals EOS models, whereas they decrease below $O(10^{-4})$ in the ideal gas EOS case at $\Delta p/p_{b,o} \geq 10^4$. Although the bubble volume diverges considerably in the final stages of collapse (Fig. 3), the collapse times remain similar across EOS models (Fig. 6b). The van der Waals EOS cases exhibit shorter collapse times than the ideal gas EOS, as the presence of a molecular hard-core volume causes the bubble to rebound earlier. The absolute value of the maximum bubble-wall velocity increases with the driving pressure ratio for all EOS models (Fig. 6c). However, for $\Delta p/p_{b,o} \geq 100$, the van der Waals EOS cases show smaller peak velocities compared to the ideal gas EOS. This reduction is attributed to weaker bubble compression, which limits the wall acceleration and thus the wall velocity. Additionally, $\max|\dot{R}|/c_l$ represents the bubble-wall Mach number [25,45,51,58], which characterizes the degree of liquid compressibility during collapse. Therefore, reduced compressibility effects are expected for the van der Waals EOS. Overall, both the full and volume-limited van der Waals EOS models show similar trends (see also Fig. 1), indicating the dominant role of finite molecular volume at high driving pressures, in contrast to the minor contribution from intermolecular attractive forces.

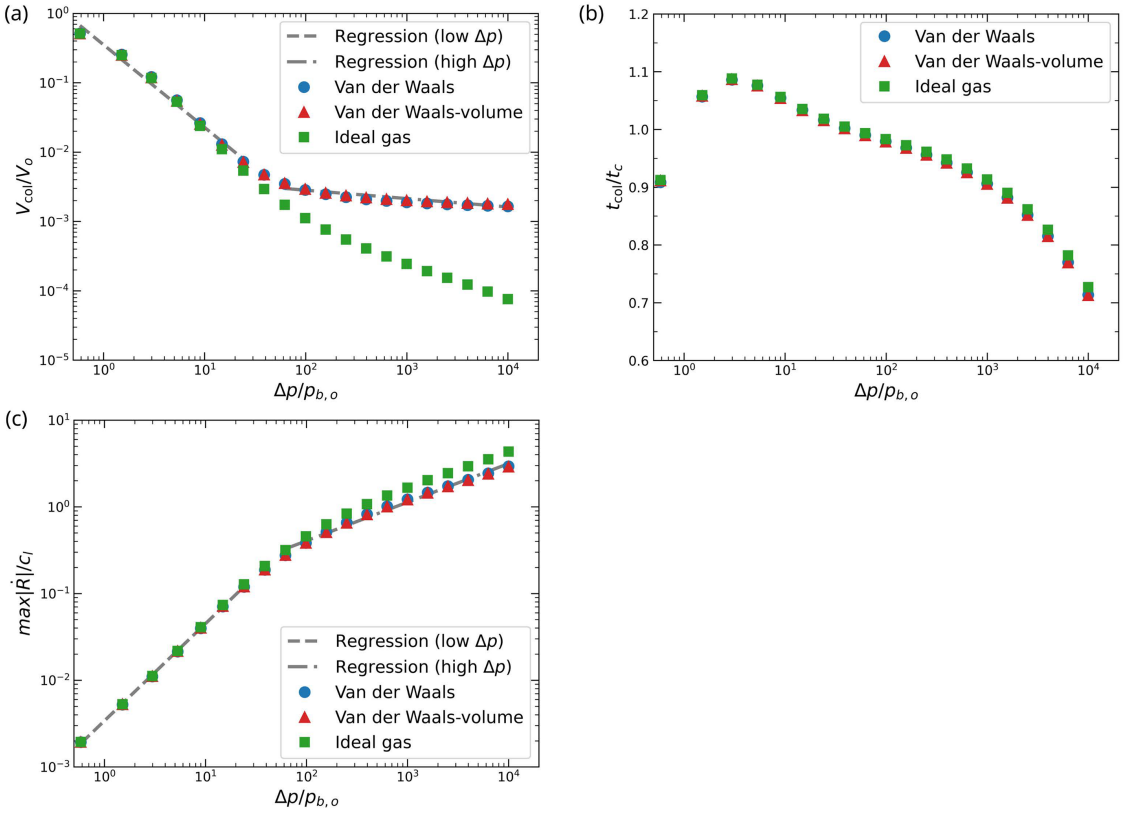

Figure 6: Bubble dynamics at collapse under different driving pressure ratios for the van der Waals and ideal gas EOS. (**a**) Minimum bubble volume at collapse, normalized by the initial volume, (**b**) collapse time, normalized by the estimated collapse time, and (**c**) absolute value of the maximum bubble-wall velocity, normalized by the speed of sound in the liquid. (Blue circles) full van der Waals EOS, (red triangles) volume-limited van der Waals EOS, and (green squares) ideal gas EOS. Fitted linear regression lines for the volume-limited van der Waals EOS case are shown as dashed (low driving pressure regime) and dash-dotted (high driving pressure regime) lines, respectively

We conduct a statistical analysis to identify the regimes where finite molecular volume effects become important. A cutoff at $\Delta p/p_{b,o} = 40$ is defined based on the peak of the absolute second derivative of the response variable, indicating a transition in bubble collapse behavior. We fit separate multivariate linear regression models for each response variable and pressure regime to evaluate how the relationship between driving pressure ratio and two key bubble dynamics (the minimum bubble volume and the maximum bubble-wall velocity) varies for different EOS models. Each model includes the driving pressure ratio, EOS (as an indicator variable), their interaction as predictors, and bubble dynamics quantities as a response variable. Both the driving pressure ratio and response variables are evaluated on a log scale.

Separate regressions for the volume-limited van der Waals EOS above and below the cutoff are shown in Fig. 6a and Fig. 6c. The cutoff data point, located near the transition, is excluded to improve the accuracy of the regression models. Both the normalized bubble volume and bubble-wall velocity scale with the driving pressure ratio as $\sim(\Delta p/p_{b,o})^{\alpha}$, where α is the fitted slope corresponding to each pressure regime and EOS. For example, the volume-limited EOS case exhibits the following behavior:

$$\frac{V_{\text{col}}}{V_0} \sim \begin{cases} \left(\dfrac{\Delta p}{p_{b,o}}\right)^{-1.192}, & \text{for low } \Delta p/p_{b,o} \\ \left(\dfrac{\Delta p}{p_{b,o}}\right)^{-0.121}, & \text{for high } \Delta p/p_{b,o} \end{cases}, \quad \frac{\max|\dot{R}|}{c_l} \sim \begin{cases} \left(\dfrac{\Delta p}{p_{b,o}}\right)^{1.120}, & \text{for low } \Delta p/p_{b,o} \\ \left(\dfrac{\Delta p}{p_{b,o}}\right)^{0.445}, & \text{for high } \Delta p/p_{b,o} \end{cases}. \tag{13}$$

We observe that the slopes across EOS cases remain similar at low driving pressures but diverge at high pressures, particularly for the minimum bubble volume. Specifically, we observe statistically significant differences in slope between the van der Waals EOS cases and the ideal gas EOS at the high pressure regime, but only minor differences at low driving pressures, as summarized in Table 2. For $\Delta p/p_{b,o} \leq 40$, the slopes estimated for the van der Waals EOS cases do not differ significantly from those of the ideal gas EOS for either the minimum bubble volume ($\alpha_{\text{ideal gas}} = -1.256$, $\alpha_{\text{van der Waals-volume}} = -1.192$, $p = 0.490$) or the maximum bubble-wall velocity ($\alpha_{\text{ideal gas}} = 1.133$, $\alpha_{\text{van der Waals-volume}} = 1.120$, $p = 0.387$). In contrast, for $\Delta p/p_{b,o} \geq 40$, there is a substantial deviation in the slopes for the minimum bubble volume ($\alpha_{\text{ideal gas}} = -0.592$, $\alpha_{\text{van der Waals-volume}} = -0.121$, $p < 10^{-3}$), and smaller but still notable differences for the maximum bubble-wall velocity ($\alpha_{\text{ideal gas}} = 0.496$, $\alpha_{\text{van der Waals-volume}} = 0.445$, $p = 0.036$). The slope and p-value for the full van der Waals EOS are similar to those of the volume-limited van der Waals EOS (Table 2). It is worth noting that the identified cutoff near $\Delta p/p_{b,o} \approx 40$ was determined as a statistical marker and validated through comparison of p-values. However, this threshold also has physical significance. The finite molecular volume effects become important when the bubble volume decreases below $V/V_o \approx 10^{-2}$ (Fig. 1), which occurs around $\Delta p/p_{b,o} \approx 40$ (Fig. 6a). Thus, the cutoff not only represents a statistically identified transition but also corresponds to the onset of finite molecular volume effects, where the non-ideal EOS cases deviate from the ideal EOS case.

Table 2: Regression results for bubble dynamics quantities for low and high driving pressure regimes. Linear regression parameters (slope and p-value) for normalized minimum bubble volume and maximum bubble-wall velocity are shown for two regimes divided at the cutoff, $\Delta p/p_{b,o} = 40$. p-values indicate statistical significance of slope differences compared to the ideal gas EOS (significance level = 0.05)

Quantities	$\Delta p/p_{b,o}$	EOS	Slope (α)	p-value for slope
V_{col}/V_o		Ideal gas	−1.256	–
	Low	Van der Waals	−1.188	0.469
		Van der Waals-volume	−1.192	0.490

(Continued)

Table 2 (continued)

Quantities	$\Delta p/p_{b,o}$	EOS	Slope (α)	p-value for slope
$\max\lvert\dot{R}/c_l\rvert$	High	Ideal gas	−0.592	–
		Van der Waals	−0.130	$<10^{-3}$
		Van der Waals-volume	−0.121	$<10^{-3}$
	Low	Ideal gas	1.133	–
		Van der Waals	1.118	0.323
		Van der Waals-volume	1.120	0.387
	High	Ideal gas	0.496	–
		Van der Waals	0.448	0.046
		Van der Waals-volume	0.445	0.036

4.2 Energy Concentration and Radiation during the Collapse Phase

Following the analysis of bubble dynamics, we examine the energy partition at collapse to understand trends in energy concentration and radiation for different driving pressure ratios (Fig. 7). We focus on the volume-limited van der Waals EOS case, which is very similar to the full model. At $\Delta p/p_{b,o} \leq 15$, the majority of the energy, approximately 80% of the total energy, is concentrated as bubble internal energy (Eq. (6) or (7)). As the driving pressure increases, both the liquid potential energy (Eq. (11)) and the bubble internal energy decrease, while the acoustic radiation energy (Eq. (10)) increases significantly. This trend corresponds with an increase in the bubble-wall Mach number, indicating stronger compressibility effects. At $\Delta p/p_{b,o} \geq 100$, more than 60% of the total energy is radiated acoustically. For very high pressure ratios, $\Delta p/p_{b,o} \geq 10^3$, the acoustic radiation energy exceeds 90% of the total energy.

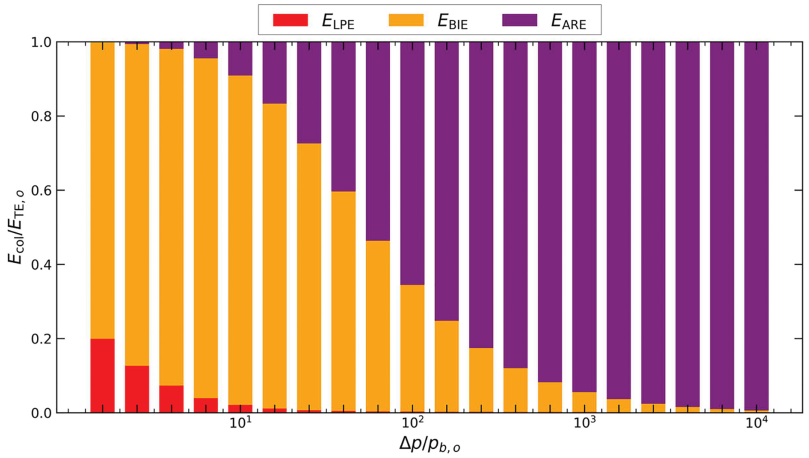

Figure 7: Energy partition at collapse for different driving pressure ratios using the volume-limited van der Waals EOS: (red bars) liquid potential energy (Eq. (11)), (orange bars) bubble internal energy (Eq. (7)), and (purple bars) acoustic radiation energy (Eq. (10))

We compare each energy component at collapse for different EOS models (Fig. 8). Overall, these models show similar trends across different driving pressure ratios: as the driving pressure increases, both the liquid potential energy (Eq. (11)) and the bubble internal energy (Eq. (6) or (7)) decrease, while the acoustic radiation energy (Eq. (10)) increases. This trend can be attributed to stronger compressibility effects at higher

driving pressures (or more intense bubble oscillations), as discussed with Fig. 7. At low driving pressure ratios, all EOS models behave similarly. However, at high driving pressure ratios, notable differences emerge between the van der Waals EOS cases and the ideal gas EOS. These differences are especially pronounced in the liquid potential energy, which becomes larger in the van der Waals cases due to the bubble being less compressed as a result of finite molecular volume. Thus, less potential energy is transferred to other components (Fig. 8a), and correspondingly, less energy is concentrated in the bubble (Fig. 8c). All EOS models exhibit similar maximum liquid kinetic energy (Eq. (12)) during collapse (Fig. 8b), since this peak occurs before the bubble is strongly compressed and finite molecular volume effects become important. Additionally, the acoustic radiation energy at collapse is comparable among the three EOS models (Fig. 8d), as the radiated energy exceeds 95% at this high driving pressure regime, despite differences in the bubble-wall Mach numbers (Fig. 6c).

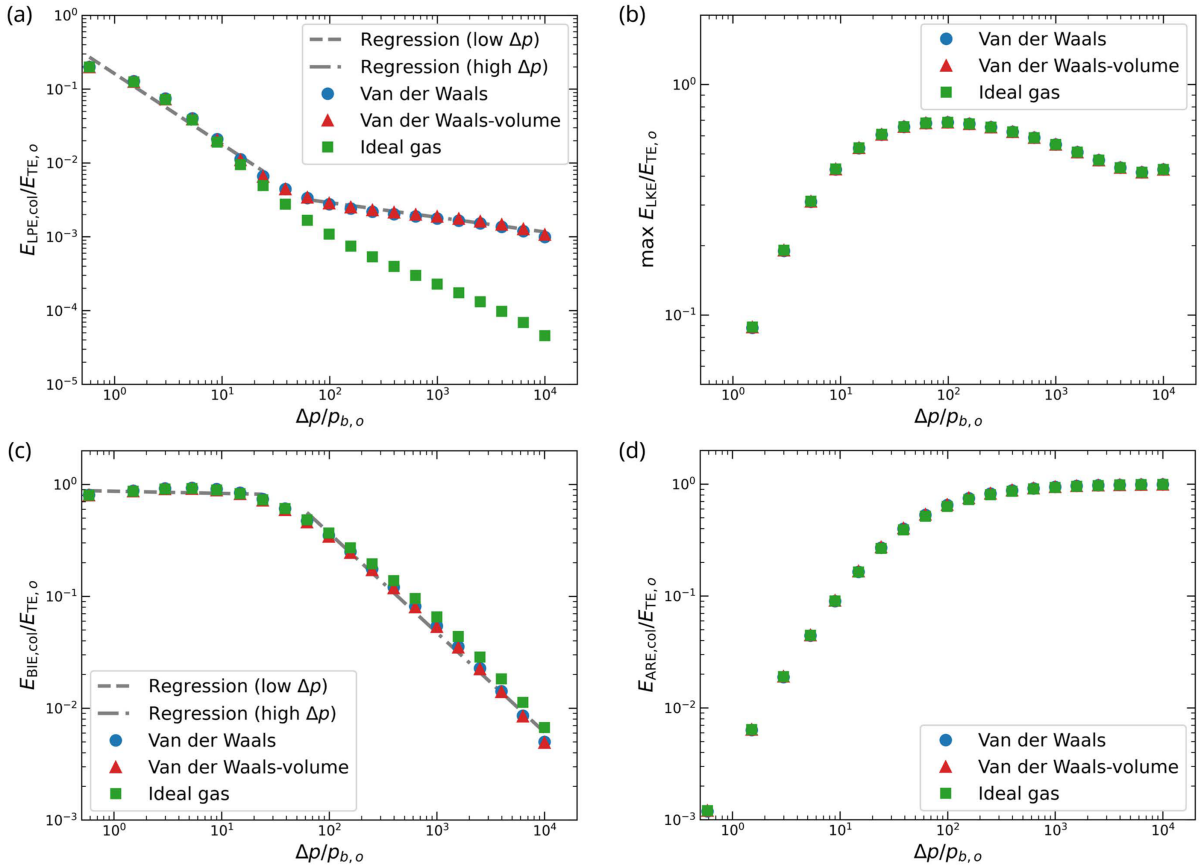

Figure 8: Energy components at collapse under different driving pressure ratios for the van der Waals and ideal gas EOS. (**a**) Liquid potential energy (Eq. (11)) at collapse, (**b**) maximum liquid kinetic energy (Eq. (12)) during collapse, (**c**) bubble internal energy (Eq. (6) or (7)) at collapse, and (**d**) acoustic radiation energy (Eq. (10)) at collapse for the (blue circles) full van der Waals EOS, (red triangles) volume-limited van der Waals EOS, and (green squares) ideal gas EOS. Fitted linear regression lines for the volume-limited van der Waals EOS case are shown as dashed (low driving pressure regime) and dash-dotted (high driving pressure regime) lines, respectively. All energy components are normalized by the total energy

Following the regression analysis used for bubble dynamics, we apply the same approach to the energy components at collapse (Table 3). Consistent with the bubble dynamics results, we find statistically significant differences in slope between the van der Waals EOS cases and the ideal gas EOS in the high

driving pressure regime, particularly for the liquid potential energy. For $\Delta p/p_{b,o} \leq 40$, the differences in slope between the van der Waals EOS cases and the ideal gas EOS are minor for the liquid potential energy ($\alpha_{\text{ideal gas}} = -1.021$, $\alpha_{\text{van der Waals-volume}} = -0.956$, $p = 0.560$). In contrast, for $\Delta p/p_{b,o} \geq 40$, significant differences are observed ($\alpha_{\text{ideal gas}} = -0.670$, $\alpha_{\text{van der Waals-volume}} = -0.199$, $p < 10^{-3}$). For the bubble internal energy, no statistically significant differences are found in either regime: $\Delta p/p_{b,o} \leq 40$ ($\alpha_{\text{ideal gas}} = -0.017$, $\alpha_{\text{van der Waals-volume}} = -0.020$, $p = 0.950$) and $\Delta p/p_{b,o} \geq 40$ ($\alpha_{\text{ideal gas}} = -0.839$, $\alpha_{\text{van der Waals-volume}} = -0.890$, $p = 0.118$). The full and volume-limited van der Waals EOS models yield similar slope estimates and p-values, as shown in Table 3.

Table 3: Regression results for energy components and energy concentration efficiency for low and high driving pressure regimes. Linear regression parameters (slope and p-value) for normalized liquid potential energy, normalized bubble internal energy, and energy concentration efficiency are shown for two regimes divided at the cutoff, $\Delta p/p_{b,o} = 40$. p-values indicate statistical significance of slope differences compared to the ideal gas EOS (significance level = 0.05)

Quantities	$\Delta p/p_{b,o}$	EOS	Slope (α)	p-value for slope
$E_{\text{LPE,col}}/E_{\text{TE},o}$	Low	Ideal gas	−1.021	–
		Van der Waals	−0.953	0.538
		Van der Waals-volume	−0.956	0.560
	High	Ideal gas	−0.670	–
		Van der Waals	−0.208	$<10^{-3}$
		Van der Waals-volume	−0.199	$<10^{-3}$
$E_{\text{BIE,col}}/E_{\text{TE},o}$	Low	Ideal gas	−0.017	–
		Van der Waals	−0.014	0.936
		Van der Waals-volume	−0.020	0.950
	High	Ideal gas	−0.839	–
		Van der Waals	−0.892	0.105
		Van der Waals-volume	−0.890	0.118
E_{eff}	Low	Ideal gas	−0.084	–
		Van der Waals	−0.087	0.926
		Van der Waals-volume	−0.087	0.931
	High	Ideal gas	−0.750	–
		Van der Waals	−0.805	$<10^{-3}$
		Van der Waals-volume	−0.803	$<10^{-3}$

Both the liquid potential energy and bubble internal energy at collapse scale with the driving pressure ratio according to a power-law relation of the form: $\sim (\Delta p/p_{b,o})^{\alpha}$. For example, the volume-limited EOS case exhibits the following behavior:

$$\frac{E_{\text{LPE,col}}}{E_{\text{TE},o}} \sim \begin{cases} \left(\frac{\Delta p}{p_{b,o}}\right)^{-0.956}, & \text{for low } \Delta p/p_{b,o} \\ \left(\frac{\Delta p}{p_{b,o}}\right)^{-0.199}, & \text{for high } \Delta p/p_{b,o} \end{cases}, \quad \frac{E_{\text{BIE,col}}}{E_{\text{TE},o}} \sim \begin{cases} \left(\frac{\Delta p}{p_{b,o}}\right)^{-0.020}, & \text{for low } \Delta p/p_{b,o} \\ \left(\frac{\Delta p}{p_{b,o}}\right)^{-0.890}, & \text{for high } \Delta p/p_{b,o} \end{cases}. \tag{14}$$

We quantify the energy concentration efficiency, shown in Fig. 9, defined as $E_{\text{eff}} = \Delta E_{\text{BIE,col}}/\Delta E_{\text{LPE,col}}$, where $\Delta E_{\text{BIE,col}} = E_{\text{BIE,col}} - E_{\text{BIE},o}$, $\Delta E_{\text{LPE,col}} = E_{\text{LPE,col}} - E_{\text{LPE},o}$. This efficiency measures the fraction of potential energy in the liquid that is concentrated into the bubble as internal energy during collapse. Overall, all EOS cases exhibit similar trends. At low driving pressure ratios, the energy concentration efficiency is close to 1, indicating that most of the initial potential energy is concentrated into bubble internal energy. In this regime, the efficiency values are nearly the same across all EOS cases. As the driving pressure ratio increases beyond the cutoff value of $\Delta p/p_{b,o} = 40$, the efficiency drops significantly, falling to about 60% just above the cutoff. With further increases in driving pressure, the efficiency decreases sharply and falls below 1% at $\Delta p/p_{b,o} = 10^4$. The van der Waals EOS models show lower energy concentration efficiencies compared to the ideal gas EOS. This can be attributed to the fact that the finite molecular volume resists compression strongly at high driving pressure, resulting in earlier bubble rebound and reduced energy concentration into the bubble.

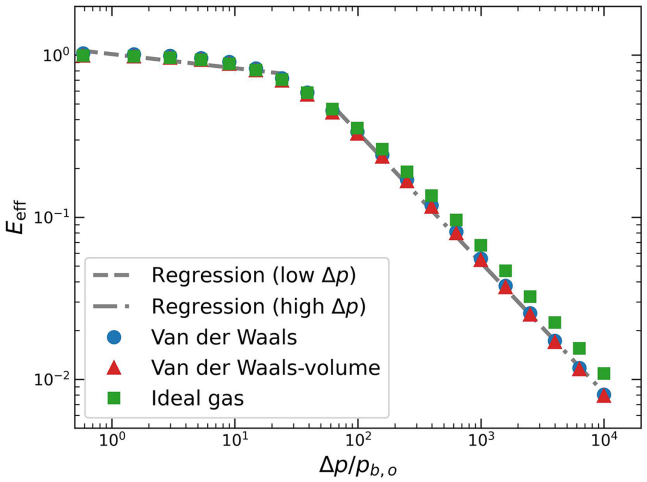

Figure 9: Energy concentration efficiency at collapse as a function of driving pressure ratio for different EOS models: (Blue circles) full van der Waals EOS, (red triangles) volume-limited van der Waals EOS, and (green squares) ideal gas EOS. Fitted linear regression lines for the volume-limited van der Waals EOS are shown as dashed (low driving pressure regime) and dash-dotted (high driving pressure regime) lines, respectively

We scale the energy concentration efficiency in the high driving pressure regime for different EOS cases to examine its dependence on the initial problem parameters. For the volume-limited van der Waals, the efficiency can be expressed as: $E_{\text{eff}} \approx (p_\infty/p_{b,o})^{-1}((V_{\text{col}} - V_{\text{van}})/V_o)^{1-\gamma}(\gamma - 1)^{-1}$. For the ideal gas EOS, the same relation applied with $V_{\text{van}} = 0$. This scaling indicates that the efficiency is primarily determined by the driving pressure ratio and the bubble compression ratio, rather than by the initial bubble radius. However, it does depend on gas properties, which determine γ and EOS parameters (a_{van}, b_{van}, V_{van}). While bubble size does not directly affect the efficiency, larger bubbles collapse more slowly, making neglected effects such as viscous and thermal conduction more important, which may indirectly reduce efficiency. At low driving pressure ratios, the initial bubble radius can also play a role, since the initial bubble internal energy and liquid potential energy are not negligible.

We apply the same regression analysis used for the energy components to determine the relationship between energy concentration efficiency and the driving pressure ratio. The estimated slopes and corresponding p-values for each driving pressure regime are summarized in Table 3. As with the energy components, no statistically significant differences are observed between van der Waals EOS cases and the ideal gas EOS in the low driving pressure regime ($\alpha_{\text{ideal gas}} = -0.084$, $\alpha_{\text{van der Waals-volume}} =$

-0.087, $p = 0.931$). However, significant differences emerge in the high driving pressure regime ($\alpha_{\text{ideal gas}} = -0.750$, $\alpha_{\text{van der Waals-volume}} = -0.803$, $p < 10^{-3}$), indicating that EOS-dependence effects become prominent at higher driving pressures. The derived scaling relationships for energy concentration efficiency using the volume-limited van der Waals EOS are:

$$E_{\text{eff}} \sim \begin{cases} \left(\dfrac{\Delta p}{p_{b,o}}\right)^{-0.087} & \text{, for low } \Delta p/p_{b,o} \\ \left(\dfrac{\Delta p}{p_{b,o}}\right)^{-0.803} & \text{, for high } \Delta p/p_{b,o} \end{cases}. \tag{15}$$

4.3 Shock Propagation during the Rebound Phase

We model the propagation of the shock during the rebound phase to investigate the relationship between the peak shock pressure and the initial driving pressure (Fig. 10). The shock pressure is estimated based on its decay rate as a function of radial distance. During strong oscillations, the rapid deceleration of the bubble wall in the final stages of collapse produces a region of very high pressure in the surrounding liquid. Such pressure leads to an outward-propagating compression wave that can steepen into a shock, followed by another compression wave during rebound due to the outward acceleration of the bubble wall [27,58]. As these waves travel outward, more recently emitted waves overtake earlier ones and eventually merge into a single shock wave, which has been observed experimentally [26,59,60]. The shock decays faster than r^{-1}, which is the decay rate expected in the acoustic limit, consistent with observations from underwater explosions [47,48,61] and cavitation bubble simulations [62]. To estimate the peak shock pressure, we employ a similitude-based scaling relation: $p_{sh} \approx p_{b,\text{col}}(R_{\text{col}}/r_{sh})^{1+k}$, where r_{sh} is the radial location of the shock peak and k is a material-dependent exponent. We adopt $k = 0.13$ [28,29,47,61], a value that has been validated against experimental observations and direct simulations by [28,29]. This empirical relation is a simplified form of the more complete Kirkwood–Bethe hypothesis-based relation for spherical shock propagation: $p_m \sim (R_{\text{col}}/r_{sh})/[\log(r_{sh}/R)]^{1/2}$ for $r \gg R$. It is worth noting that experimental studies in both biomedical [63] and hydrodynamic contexts [11,41,64] have measured shock waves from cavitation bubble collapse, confirming the production of sharp, high-amplitude shock fronts, consistent with our formulation for peak shock pressure estimation. As a reference case, the peak pressure under the acoustic approximation, which decays as r^{-1}, is also provided, representing conditions at low driving pressure ratios where the bubble collapse is non-violent.

The shock pressure normalized by the initial bubble pressure shows very similar trends across all EOS models (Fig. 10a), whereas noticeable deviations arise when the shock pressure is normalized by the driving pressure (Fig. 10b). This difference is due to the choice of reference for normalization: the initial bubble pressure is much smaller than the shock pressure, which masks differences between the van der Waals EOS cases and ideal gas EOS in Fig. 10a. However, when normalized by the driving pressure, these differences become more pronounced (Fig. 10b). $p_{sh}/p_{b,o}$ increases monotonically with the driving pressure ratio, although its growth rate decreases in the high driving pressure regime where compressibility effects become significant and acoustic radiation energy accounts for a substantial portion of the total energy (Fig. 10a). However, $p_{sh}/\Delta p$ peaks near the cutoff at $\Delta p/p_{b,o} \approx 40$ and decreases at higher driving pressure ratios. In this regime, increased compression and elevated bubble-wall velocities enhance compressibility effects and lead to greater acoustic radiation energy. As a result, less energy is concentrated in the bubble, resulting in lower shock pressures relative to the imposed driving pressure. Additionally, the value of $p_{sh}/\Delta p$ is higher in the van der Waals EOS cases than in the ideal gas EOS, as the actual bubble pressure at collapse is higher in the van der Waals EOS cases due to the finite molecular volume. The peak pressure in the acoustic

approximation case is relatively higher than the estimated peak shock pressure (Fig. 10) because the shock decays more rapidly than acoustic waves as it propagates.

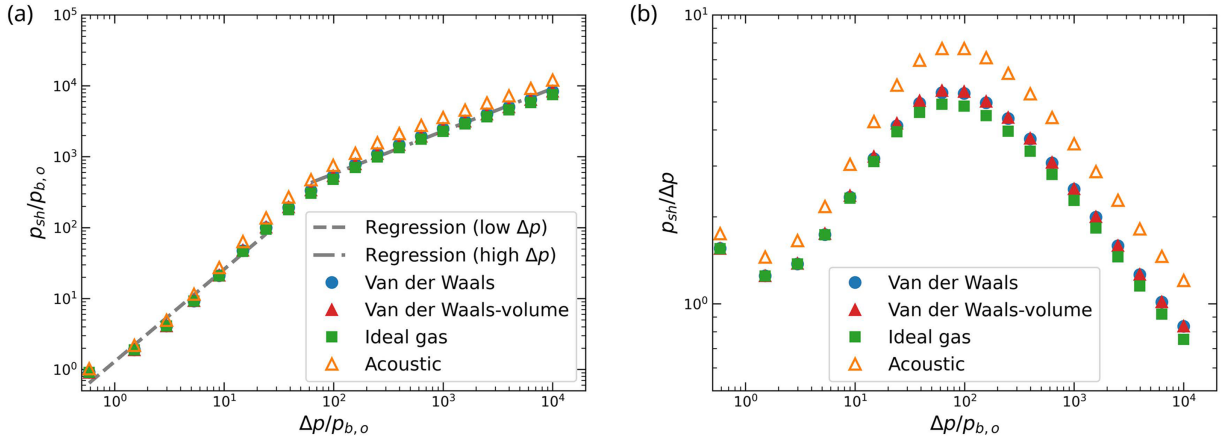

Figure 10: Estimated shock pressures at $r = 2R_o$ as a function of the driving pressure ratio for different EOS models. Shock pressure is normalized by (**a**) the initial bubble pressure $p_{b,o}$ and (**b**) the driving pressure Δp: (Blue circles) full van der Waals EOS, (red triangles) volume-limited van der Waals EOS, and (green squares) ideal gas EOS. Fitted linear regression lines for the volume-limited van der Waals EOS are shown as dashed (low driving pressure regime) and dash-dotted (high driving pressure regime) lines. For reference, the acoustic approximation case is also provided (orange hollow triangles)

We perform a statistical analysis for $p_{sh}/p_{b,o}$, which shows a linear relationship with the driving pressure ratio in log-log scale, as summarized in Table 4. Overall, the estimated slopes for $p_{sh}/p_{b,o}$ are similar between the van der Waals EOS cases and the ideal gas EOS for both low and high driving pressure regimes ($\alpha \approx 1.30$ and $\alpha = 0.60$, respectively), with p-values around 0.9, indicating no statistically significant differences. This reflects their comparable behavior at each regime (Fig. 10a). The derived scaling relationships for shock pressure using the volume-limited van der Waals EOS are:

$$\frac{p_{sh}}{p_{b,o}} \sim \begin{cases} \left(\dfrac{\Delta p}{p_{b,o}}\right)^{1.302} & \text{, for low } \Delta p/p_{b,o} \\ \left(\dfrac{\Delta p}{p_{b,o}}\right)^{0.602} & \text{, for high } \Delta p/p_{b,o} \end{cases}. \tag{16}$$

Table 4: Regression results for shock pressure at $r = 2R_o$, normalized by the initial bubble pressure, for low and high driving pressure regimes. Linear regression parameters (slope and p-value) are shown for each regime, divided at the cutoff, $\Delta p/p_{b,o} = 40$. p-values indicate the statistical significance of slope differences compared to the ideal gas EOS (significance level = 0.05)

Quantities	$\Delta p/p_{b,o}$	EOS	Slope (α)	p-value for slope
$p_{sh}/p_{b,o}$	Low	Ideal gas	1.285	–
		Van der Waals	1.295	0.927
		Van der Waals-volume	1.302	0.883
	High	Ideal gas	0.606	–
		Van der Waals	0.605	0.983
		Van der Waals-volume	0.602	0.899

5 Conclusion

We propose a novel energy budget framework to evaluate the energy components of the bubble–liquid system during strong oscillations of a spherical bubble, where molecular effects become important. We derive expressions for the internal energy of the bubble and the corresponding acoustic radiation energy, both of which strongly depend on the choice of EOS, while ensuring strict conservation of total energy in the system. This framework enables, for the first time, a systematic comparison of how non-ideal EOS (the van der Waals and its volume-limited form) alter bubble compression, energy redistribution, and shock emission relative to the ideal gas EOS. By modeling an oscillation in two stages, the collapse phase (from the initial state to the minimum radius) and the rebound phase (including shock generation), we link EOS-dependent energy transfer directly to peak shock pressures. Through statistical analysis across a wide range of driving pressures, we further identify distinct low- and high-pressure regimes and characterize the differences in behavior between the van der Waals EOS and the ideal gas EOS in these regimes. We also establish new scaling relations that connect the driving pressure ratio to bubble dynamics, energy concentration, and peak shock pressure. These contributions provide new insights into the role of molecular effects in cavitation dynamics and deliver predictive tools for anticipating cavitation-induced energy transfer in practical applications.

We observe significant differences between the van der Waals and ideal gas EOS cases at high driving pressure ratios, where intense compression leads to strong finite molecular volume effects. Compared to the ideal gas EOS, the van der Waals EOS cases exhibit much less compression, by orders of magnitude, along with lower bubble-wall velocity (and bubble-wall Mach number), indicating reduced compressibility effects. To quantify these differences, we conduct statistical analyses for both low and high driving pressure regimes, separated by a cutoff pressure ratio of 40. The resulting p-values reveal substantial differences between EOS models in the high driving pressure regime, particularly in the bubble volume at collapse.

We quantify the energy components of the bubble–liquid system using our energy budget framework, tailored to each EOS model. At low driving pressure ratios, most of the initial energy is concentrated to the bubble, whereas at high driving pressures, the majority of the energy is radiated away as acoustic waves. In the van der Waals EOS cases, a smaller portion of the potential energy is transferred to other energy components, resulting in reduced energy concentration to the bubble. We also compute the energy concentration efficiency, which is consistently lower for the van der Waals EOS cases, especially at higher driving pressures. Both the full and volume-limited van der Waals EOS models yield similar results, suggesting that intermolecular attractive forces play a minor role in bubble dynamics and energy transfer within the given driving pressure range. In addition, we estimate the shock peak pressure at a fixed radial distance from the bubble center. This pressure increases when normalized by the initial bubble pressure but decreases when normalized by the driving pressure at high driving pressure ratios, due to reduced energy concentration in the bubble. Finally, we derive scaling relations using linear regression for key quantities, including minimum bubble volume, bubble-wall velocity, liquid potential energy, bubble internal energy, energy concentration efficiency, and shock pressure, as functions of the driving pressure ratio. These relations provide practical insights for predicting cavitation bubble dynamics, energy concentration, and shock pressure in simulations and applications.

Future Direction

In the present study, the liquid is modeled as weakly compressible using the Keller–Miksis formulation, which captures first-order compressibility effects with the small dimensionless parameter ε, enabling the modeling of acoustic wave propagation. This weakly compressible formulation captures most of the collapse dynamics; however, highly nonlinear bubble behavior and shock formation can be more accurately resolved using high-order compressible flow models, such as the Gilmore equation [65] or direct numerical

simulations [28,29]. To account for shock propagation, we employ a similitude-based scaling relation that shows good agreement with direct simulation results for driving pressure ratios between 280 and 2,800 [28], which fall within the high-pressure regime analyzed in this study. At lower driving pressure ratios, the collapse is relatively gentle, producing weak pressure waves that decay as $1/r$, consistent with linear acoustic propagation. Fig. 10 includes an acoustic approximation to represent this regime. To rigorously capture the transition between acoustic to shock-emitted regimes, more advanced approaches, such as the method of characteristics, Kirkwood–Bethe hypothesis-based analyses [66,67], or fully compressible direct numerical simulations [62], would be needed. While such modeling is beyond the scope of the present study, it represents an important direction for future research.

The developed energy budget framework has potential to be applied to a variety of complex bubble–liquid systems, including bubbles near boundaries with geometric constraints [19,68–70], thermodynamic effects [71], bubble clouds [23,24,72], and viscoelastic media [73,74]. In particular, under strong oscillations, the non-ideal gas formulation could be extended to incorporate thermal effects and phase change, enabling a more comprehensive quantification of energy transfer. These effects may interact non-trivially with non-ideal EOS behavior, especially at high pressures; while violent (or inertial) collapse occurs too rapidly for significant vapor diffusion or condensation [43], the extreme temperatures reached [7,32] suggest that thermal conduction and phase change could still influence energy redistribution. The framework can also be extended to account for viscous dissipation at the bubble wall, which becomes significant for larger bubbles with slower growth and collapse. In such regimes, the work done by the pressure difference across the interface is dissipated through normal viscous stresses, contributing to energy loss. In addition, the developed framework can be applicable to the weakly non-spherical bubble oscillations [52]. In this case, the bubble internal energy still follows Eqs. (6) and (7), since it depends on the total bubble volume, whereas both the liquid kinetic energy and the acoustic radiation energy would need modification due to perturbation in the velocity potential [75]. The framework may further be applied to spherical bubble-bubble interactions, which are especially relevant in bubble cloud dynamics. In addition, the spherical formulation can be adapted to non-spherical bubble oscillations, where asymmetry becomes pronounced, affecting the energy transfer. By incorporating the elastic energy stored in the surrounding medium, the framework can also be extended to quantify energy modes in viscoelastic environments. In this context, this work lays a foundation for elucidating energy transfer, concentration, and radiation in bubble dynamics problems under more realistic settings.

Acknowledgement: None.

Funding Statement: This work was supported by Institute of Information & Communications Technology Planning & Evaluation (IITP) grant funded by the Korea government (MSIT) (No. RS-2022-00155966, Artificial Intelligence Convergence Innovation Human Resources Development (Ewha Womans University)).

Author Contributions: The authors confirm contribution to the paper as follows: Conceptualization, Minki Kim, Jenny Jyoung Lee; methodology, Minki Kim, Jenny Jyoung Lee; software, Jenny Jyoung Lee; validation, Minki Kim; formal analysis, Minki Kim, Jenny Jyoung Lee; investigation, Minki Kim; writing—original draft preparation, Minki Kim; writing—review and editing, Minki Kim, Jenny Jyoung Lee; supervision, Jenny Jyoung Lee; project administration, Jenny Jyoung Lee; funding acquisition, Jenny Jyoung Lee. All authors reviewed the results and approved the final version of the manuscript.

Availability of Data and Materials: The simulation data that support the findings of this study, along with the R code used for statistical analysis, are openly available in the GitHub repository: https://github.com/mkkim400/Regression-analysis-bubble-dynamics (accessed on 15 September 2025). The authors confirm that the data supporting the findings of this study are available within the article.

Ethics Approval: Not applicable.

Conflicts of Interest: The authors declare no conflicts of interest to report regarding the present study.

References

1. Arndt RE. Cavitation in fluid machinery and hydraulic structures. Annu Rev Fluid Mech. 1981;13(1):273–326. doi:10.1146/annurev.fl.13.010181.001421.
2. Yang J, Lee KH, Lee CH. Research on cavitation characteristics and influencing factors of herringbone gear pump. Comput Model Eng Sci. 2024;139(3):2917–46. doi:10.32604/cmes.2024.046740.
3. Peng D, Chen G, Yan J, Wang S. Numerical investigation of the Angle of Attack effect on cloud cavitation flow around a Clark-Y hydrofoil. Comput Model Eng Sci. 2024;139(3):2947–64. doi:10.32604/cmes.2024.047265.
4. Khokhlova VA, Fowlkes JB, Roberts WW, Schade GR, Xu Z, Khokhlova TD, et al. Histotripsy methods in mechanical disintegration of tissue: towards clinical applications. Int J Hyperthermia. 2015;31(2):145–62. doi:10.3109/02656736.2015.1007538.
5. Johnsen E, Colonius T. Shock-induced collapse of a gas bubble in shockwave lithotripsy. J Acoust Soc Am. 2008;124(4):2011–20. doi:10.1121/1.2973229.
6. Brennen CE. Cavitation in medicine. Interface Focus. 2015;5(5):20150022. doi:10.1098/rsfs.2015.0022.
7. Suslick KS, Flannigan DJ. Inside a collapsing bubble: sonoluminescence and the conditions during cavitation. Annu Rev Phys Chem. 2008;59(1):659–83. doi:10.1146/annurev.physchem.59.032607.093739.
8. Mauri G, Nicosia L, Xu Z, Di Pietro S, Monfardini L, Bonomo G, et al. Focused ultrasound: tumour ablation and its potential to enhance immunological therapy to cancer. Br J Radiol. 2018;91(1083):20170641. doi:10.1259/bjr.20170641.
9. Man VH, Li MS, Derreumaux P, Wang J, Nguyen TT, Nangia S, et al. Molecular mechanism of ultrasound interaction with a blood brain barrier model. J Chem Phys. 2020;153(4):045104.
10. Nguyen PH. Modeling stable cavitation of coated microbubbles: a framework integrating smoothed dissipative particle dynamics and the Rayleigh-Plesset equation. J Chem Phys. 2024;161(6):64110. doi:10.1063/5.0220395.
11. Vogel A, Lauterborn W, Timm R. Optical and acoustic investigations of the dynamics of laser-produced cavitation bubbles near a solid boundary. J Fluid Mech. 1989;206:299–338. doi:10.1017/s0022112089002314.
12. Tomita Y, Robinson P, Tong R, Blake J. Growth and collapse of cavitation bubbles near a curved rigid boundary. J Fluid Mech. 2002;466:259–83. doi:10.1017/s0022112002001209.
13. Beig S, Aboulhasanzadeh B, Johnsen E. Temperatures produced by inertially collapsing bubbles near rigid surfaces. J Fluid Mech. 2018;852:105–25. doi:10.1017/jfm.2018.525.
14. Karimi A, Martin J. Cavitation erosion of materials. Int Met Rev. 1986;31(1):1–26.
15. Plesset MS, Prosperetti A. Bubble dynamics and cavitation. Annu Rev Fluid Mech. 1977;9(1):145–85. doi:10.1146/annurev.fl.09.010177.001045.
16. Zeng Q, Gonzalez-Avila SR, Dijkink R, Koukouvinis P, Gavaises M, Ohl CD. Wall shear stress from jetting cavitation bubbles. J Fluid Mech. 2018;846:341–55. doi:10.1017/jfm.2018.286.
17. Zeng Q, An H, Ohl CD. Wall shear stress from jetting cavitation bubbles: influence of the stand-off distance and liquid viscosity. J Fluid Mech. 2022;932:A14. doi:10.1017/jfm.2021.997.
18. Blake JR, Gibson D. Cavitation bubbles near boundaries. Annu Rev Fluid Mech. 1987;19(1):99–123. doi:10.1146/annurev.fl.19.010187.000531.
19. Rodriguez M Jr, Beig SA, Barbier CN, Johnsen E. Dynamics of an inertially collapsing gas bubble between two parallel, rigid walls. J Fluid Mech. 2022;946:A43. doi:10.1017/jfm.2022.571.
20. White W, Beig SA, Johnsen E. Pressure fields produced by single-bubble collapse near a corner. Phys Rev Fluids. 2023;8(2):23601. doi:10.1103/physrevfluids.8.023601.
21. Nguyen VT, Sagar HJ, el Moctar O, Park WG. Understanding cavitation bubble collapse and rebound near a solid wall. Int J Mech Sci. 2024;278:109473. doi:10.1016/j.ijmecsci.2024.109473.
22. Nguyen QT, Nguyen VT, Sagar H, Moctar O, Park WG. Effects of oscillating curved wall on behavior of a collapsing cavitation bubble. Phys Fluids. 2025;37(1):013312. doi:10.1063/5.0245434.

23. Ando K, Colonius T, Brennen CE. Numerical simulation of shock propagation in a polydisperse bubbly liquid. Int J Multiph Flow. 2011;37(6):596–608. doi:10.1016/j.ijmultiphaseflow.2011.03.007.
24. Maeda K, Colonius T. Bubble cloud dynamics in an ultrasound field. J Fluid Mech. 2019;862:1105–34. doi:10.1017/jfm.2018.968.
25. Holzfuss J. Acoustic energy radiated by nonlinear spherical oscillations of strongly driven bubbles. Proc R Soc A Math Phys Eng Sci. 2010;466(2118):1829–47. doi:10.1098/rspa.2009.0594.
26. Tinguely M, Obreschkow D, Kobel P, Dorsaz N, De Bosset A, Farhat M. Energy partition at the collapse of spherical cavitation bubbles. Phys Rev E. 2012;86(4):46315. doi:10.1103/physreve.86.046315.
27. Liang X-X, Linz N, Freidank S, Paltauf G, Vogel A. Comprehensive analysis of spherical bubble oscillations and shock wave emission in laser-induced cavitation. J Fluid Mech. 2022;940:A5. doi:10.1017/jfm.2022.202.
28. Kim M. Energy transport during growth and collapse of a cavitation bubble [Ph.D. thesis]. Ann Arbor, MI, USA: University of Michigan; 2022.
29. Kim M, Beig SA, Johnsen E. Energy concentration and release during the inertial collapse of a spherical gas cavity in a liquid. Phys Rev Fluids. 2025;10(9):214. doi:10.1103/bqyr-5c1d.
30. Löfstedt R, Barber BP, Putterman SJ. Toward a hydrodynamic theory of sonoluminescence. Phys Fluids. 1993;5(11):2911–28. doi:10.1063/1.858700.
31. Kerboua K, Hamdaoui O. Computational study of state equation effect on single acoustic cavitation bubble's phenomenon. Ultrason Sonochem. 2017;38:174–88. doi:10.1016/j.ultsonch.2017.03.005.
32. Didenko YT, Suslick KS. The energy efficiency of formation of photons, radicals and ions during single-bubble cavitation. Nature. 2002;418(6896):394–7. doi:10.1038/nature00895.
33. Flannigan DJ, Hopkins SD, Camara CG, Putterman SJ, Suslick KS. Measurement of pressure and density inside a single sonoluminescing bubble. Phys Rev Lett. 2006;96(20):204301. doi:10.1103/physrevlett.96.204301.
34. Flannigan DJ, Suslick KS. Plasma formation and temperature measurement during single-bubble cavitation. Nature. 2005;434(7029):52–5. doi:10.1038/nature03361.
35. Brenner MP, Hilgenfeldt S, Lohse D. Single-bubble sonoluminescence. Rev Mod Phys. 2002;74(2):425. doi:10.1103/revmodphys.74.425.
36. Brennen CE. Cavitation and bubble dynamics. Cambridge, UK: Cambridge University Press; 2014.
37. Leighton TG. An introduction to acoustic cavitation. In: Ultrasound in medicine. Boca Raton, FL, USA: CRC Press; 2020. p. 199–224.
38. Lu X, Prosperetti A, Toegel R, Lohse D. Harmonic enhancement of single-bubble sonoluminescence. Phys Rev E. 2003;67(5):56310. doi:10.1103/physreve.67.056310.
39. Rayleigh L. VIII. On the pressure developed in a liquid during the collapse of a spherical cavity. Phil Mag Or Philos Mag. 1917;34(200):94–8.
40. Keller JB, Miksis M. Bubble oscillations of large amplitude. J Acoust Soc Am. 1980;68(2):628–33. doi:10.1121/1.384720.
41. Lauterborn W, Kurz T. Physics of bubble oscillations. Rep Prog Phys. 2010;73(10):106501.
42. Storey BD, Szeri AJ. Mixture segregation within sonoluminescence bubbles. J Fluid Mech. 1999;396:203–21. doi:10.1017/s0022112099005984.
43. Storey BD, Szeri AJ. Water vapour, sonoluminescence and sonochemistry. Proc R Soc A Math Phys Eng Sci. 2000;456(1999):1685–709. doi:10.1098/rspa.2000.0582.
44. Barajas C, Johnsen E. The effects of heat and mass diffusion on freely oscillating bubbles in a viscoelastic, tissue-like medium. J Acoust Soc Am. 2017;141(2):908–18. doi:10.1121/1.4976081.
45. Hickling R, Plesset MS. Collapse and rebound of a spherical bubble in water. Phys Fluids. 1964;7(1):7–14. doi:10.1063/1.1711058.
46. Ohl C, Ikink R. Shock-wave-induced jetting of micron-size bubbles. Phys Rev Lett. 2003;90(21):214502. doi:10.1103/physrevlett.90.214502.
47. Cole RH. Underwater explosions. Princeton, NJ, USA: Princeton University Press; 1948.
48. Hunter KS, Geers TL. Pressure and velocity fields produced by an underwater explosion. J Acoust Soc Am. 2004;115(4):1483–96. doi:10.1121/1.1648680.

49. Qin Y, Wang Y, Wang Z, Yao X. The influence of various structure surface boundary conditions on pressure characteristics of underwater explosion. Comput Model Eng Sci. 2021;126(3):1093–123. doi:10.32604/cmes.2021.012969.
50. Cash JR, Karp AH. A variable order Runge-Kutta method for initial value problems with rapidly varying right-hand sides. ACM Trans Math Softw. 1990;16(3):201–22. doi:10.1145/79505.79507.
51. Prosperetti A, Lezzi A. Bubble dynamics in a compressible liquid. Part 1. First-order theory. J Fluid Mech. 1986;168:457–78. doi:10.1017/s0022112086000460.
52. Plesset M. On the stability of fluid flows with spherical symmetry. J Appl Phys. 1954;25(1):96–8 doi: 10.1063/1.1721529.
53. Burke WL. Runaway solutions: remarks on the asymptotic theory of radiation damping. Phys Rev A. 1970;2(4):1501. doi:10.1103/physreva.2.1501.
54. Templin JD. Radiation reaction and runaway solutions in acoustics. Am J Phys. 1999;67(5):407–13.
55. Arons AB, Yennie D. Energy partition in underwater explosion phenomena. Rev Mod Phys. 1948;20(3):519. doi:10.1103/revmodphys.20.519.
56. Wang Q. Local energy of a bubble system and its loss due to acoustic radiation. J Fluid Mech. 2016;797:201–30. doi:10.1017/jfm.2016.281.
57. Kirkwood JG, Bethe HA. The pressure wave produced by an underwater explosion. In: OSRD report. Washington, DC, USA: USA Office Sci Res Dev; 1942.
58. Yasui K. Acoustic cavitation. In: Acoustic cavitation and bubble dynamics. Cham, Switzerland: Springer; 2017. p. 1–35.
59. Holzfuss J, Rüggeberg M, Billo A. Shock wave emissions of a sonoluminescing bubble. Phys Rev Lett. 1998;81(24):5434. doi:10.1103/physrevlett.81.5434.
60. Garen W, Hegedűs F, Kai Y, Koch S, Meyerer B, Neu W, et al. Shock wave emission during the collapse of cavitation bubbles. Shock Waves. 2016;26(4):385–94. doi:10.1007/s00193-015-0614-z.
61. Geers TL, Hunter KS. An integrated wave-effects model for an underwater explosion bubble. J Acoust Soc Am. 2002;111(4):1584–601. doi:10.1121/1.1458590.
62. Aganin AA, Mustafin IN. Outgoing shock waves at collapse of a cavitation bubble in water. Int J Multiph Flow. 2021;144(5):103792. doi:10.1016/j.ijmultiphaseflow.2021.103792.
63. Yeats E, Lu N, Sukovich JR, Xu Z, Hall TL. Soft tissue aberration correction for histotripsy using acoustic emissions from cavitation cloud nucleation and collapse. Ultrasound Med Biol. 2023;49(5):1182–93. doi:10.1016/j.ultrasmedbio.2023.01.004.
64. Isselin JC, Alloncle AP, Autric M. On laser induced single bubble near a solid boundary: contribution to the understanding of erosion phenomena. J Appl Phys. 1998;84(10):5766–71. doi:10.1063/1.368841.
65. Gilmore FR. The growth or collapse of a spherical bubble in a viscous compressible liquid; Pasadena, CA, USA: California Institute of Technology; 1952. Report No.: 26–4.
66. Denner F, Schenke S. Modeling acoustic emissions and shock formation of cavitation bubbles. Phys Fluids. 2023;35(1):12114. doi:10.1063/5.0131930.
67. Denner F. The Kirkwood-Bethe hypothesis for bubble dynamics, cavitation, and underwater explosions. Phys Fluids. 2024;36(5):051302. doi:10.1063/5.0209167.
68. Zeng Q, Gonzalez-Avila SR, Ohl CD. Splitting and jetting of cavitation bubbles in thin gaps. J Fluid Mech. 2020;896:A28. doi:10.1017/jfm.2020.356.
69. Bhola S, Rodriguez M Jr, Beig SA, Barbier CN, Johnsen E. Inertial collapse of a gas bubble in a shear flow near a rigid wall. J Fluid Mech. 2025;1004:A3. doi:10.1017/jfm.2024.1146.
70. Nguyen QT, Kadivar E, Phan TH, Nguyen VT, el Moctar O, Park WG. Effects of free surface on dynamics of a laser-induced cavitation bubble near horizontal rigid wall. Ocean Eng. 2025;319(3):120258. doi:10.1016/j.oceaneng.2024.120258.
71. Mancia L, Rodriguez M, Sukovich J, Xu Z, Johnsen E. Single-bubble dynamics in histotripsy and high-amplitude ultrasound: modeling and validation. Phys Med Biol. 2020;65(22):225014. doi:10.1088/1361-6560/abb02b.

72. Bryngelson SH, Schmidmayer K, Colonius T. A quantitative comparison of phase-averaged models for bubbly, cavitating flows. Int J Multiph Flow. 2019;115(6):137–43. doi:10.1016/j.ijmultiphaseflow.2019.03.028.
73. Murakami K, Gaudron R, Johnsen E. Shape stability of a gas bubble in a soft solid. Ultrason Sonochem. 2020;67:105170. doi:10.1016/j.ultsonch.2020.105170.
74. Murakami K, Yamakawa Y, Zhao J, Johnsen E, Ando K. Ultrasound-induced nonlinear oscillations of a spherical bubble in a gelatin gel. J Fluid Mech. 2021;924:A38. doi:10.1017/jfm.2021.644.
75. Harkin AA, Kaper TJ, Nadim A. Energy transfer between the shape and volume modes of a nonspherical gas bubble. Phys Fluids. 2013;25(6):62101. doi:10.1063/1.4807392.